

Control of the Liouvillian gap in the finite open quantum system

Kai-Li Li(李凯丽), Yan-Sheng Liu(刘延盛), and Xi-Zheng Zhang(张禧征)
Citation: Chin. Phys. B, 2026, 35 (**1**): 010306. DOI: 10.1088/1674-1056/adeb60
http://cpb.iphy.ac.cn; http://iopscience.iop.org/cpb

What follows is a list of articles you may be interested in

PT-symmetry phase transition in a bipartite lattice with long-range interactions

Dapeng Zheng(郑大鹏), Siwu Li(李思吾), and Zeliang Xiang(项泽亮)
Chin. Phys. B, 2025, 34 (**11**): 110305. DOI: 10.1088/1674-1056/addcd4

Non-quantized Zak phases, PT/APT symmetry transitions, and doubly degenerate exceptional points in a non-Hermitian spin-orbit coupled SSH model

Jun-Xing Huo(霍俊行), Jian Li(李健), Qing-Xu Li(李清旭), and Jia-Ji Zhu(朱家骥)
Chin. Phys. B, 2025, 34 (**7**): 070301. DOI: 10.1088/1674-1056/adc7f3

Dynamics of quantum discord and geometric quantum discord in multiqubit interacting system

Xiao-Di Cheng(程晓迪), Ya-Jun Zheng(郑雅君), Meng-Jie Ran(冉梦杰), and Xiao-Yun Wang(王小云)
Chin. Phys. B, 2025, 34 (**5**): 050309. DOI: 10.1088/1674-1056/adca16

Investigating maximal steered coherence under the common impacts of reservoir and noise

Ling-Ling Xing(邢玲玲), Huan Yang(杨欢), and Gang Zhang(张刚)
Chin. Phys. B, 2025, 34 (**5**): 050304. DOI: 10.1088/1674-1056/adbbc2

Sudden change of interferometric power for X-shape states

Dian Zhu(朱典), Fu-Lin Zhang(张福林), and Jing-Ling Chen(陈景灵)
Chin. Phys. B, 2025, 34 (**2**): 020305. DOI: 10.1088/1674-1056/ad9732

Control of the Liouvillian gap in the finite open quantum system

Kai-Li Li(李凯丽), Yan-Sheng Liu(刘延盛), and Xi-Zheng Zhang(张禧征)†

College of Physics and Materials Science, Tianjin Normal University, Tianjin 300387, *China*

(Received 10 May 2025; revised manuscript received 20 June 2025; accepted manuscript online 3 July 2025)

Relaxation processes in quantum systems coupled to external environments represent one of the most fundamental nonequilibrium phenomena in condensed matter physics. The Lindblad master equation provides a powerful framework for characterizing such open quantum dynamics. In this work, we systematically investigate how different types of quantum jump operators and system geometries influence the Liouvillian gap and the properties of the nonequilibrium steady state (NESS) in finite-size systems. We demonstrate that, due to the intricate structure of the Liouvillian superoperator, multiple NESSs with unphysical characteristics can emerge. The physically meaningful steady state must instead be understood as a superposition of these NESSs that collectively satisfy the required physical constraints. Furthermore, we find that the Liouvillian gap does not necessarily increase monotonically with the system–environment coupling strength. Instead, it can exhibit a nontrivial peak structure, corresponding to a minimum in the relaxation time. The magnitude of this peak is closely related to the symmetry properties of the system. Our results provide a deeper understanding of nonequilibrium behavior in finite quantum systems and offer new insights into the design and control of open quantum dynamics.

Keywords: Liouvillian gap, nonequilibrium steady state, quantum jump operator

PACS: 03.65.Yz, 03.65.–w, 03.65.Aa

DOI: 10.1088/1674-1056/adeb60 **CSTR:** 32038.14.CPB.adeb60

1. Introduction

Recently, breakthroughs in quantum-simulation platforms ranging from ultracold atoms in optical lattices to superconducting qubit arrays have brought the nonequilibrium dynamics of open lattice systems into sharp experimental focus.[1–6] By engineering controlled coupling to external reservoirs, these experiments access regimes in which coherent many-body evolution competes directly with dissipation and quantum jumps, enabling the observation of relaxation, decoherence, and environment-induced transitions far from thermal equilibrium.[7–11]

Open quantum lattices display a wealth of phenomena with no counterpart in closed systems. Dissipation can stabilize pure or mixed steady states that defy equilibrium classification, generate long-range coherence via reservoir engineering, and induce topological phases protected by nonunitary symmetries.[12–15] Crucially, the long-time behavior is governed by the spectrum of the Liouvillian superoperator, which serves as the generator of the Lindblad master equation. Of particular importance is the Liouvillian gap, defined as the magnitude of the real part of the first nonzero eigenvalue. This gap determines the characteristic relaxation time toward the nonequilibrium steady state (NESS) and closes at dissipative critical points, indicating dynamical phase transitions and critical slowing down.[16–18]

For many-body quantum systems, the central challenge lies in the exponential growth of the Hilbert space. Each additional degree of freedom, whether in particle number or lattice size, leads to an exponential increase in the dimension of the quantum state space. This fundamental scaling severely limits both analytical tractability and experimental feasibility. As a result, studying few-site systems has become a natural and necessary approach. These small-size lattices not only offer computational and experimental accessibility but also exhibit heightened sensitivity to system parameters, enabling detailed exploration of open-system dynamics. In finite lattices, the coexistence of multiple zero modes, boundary-condition–dependent spectral singularities, and non-Hermitian skin effects further complicates the selection and physicality of the NESS. A systematic understanding of how dissipation configuration, symmetry, and boundaries conspire to shape both the NESS and the relaxation spectrum is therefore essential for controlling open-system dynamics and exploiting dissipation as a resource.

In this work, we undertake a comprehensive study of Liouvillian-gap engineering in finite one-dimensional fermionic lattices subject to Lindblad dissipation. We classify and analyze three key aspects.

(i) Jump-operator type and placement: we compare on-site dephasing and directional incoherent hopping, and vary their distribution (single-site, multi-site, and full-lattice).

(ii) Boundary conditions: we contrast open with periodic geometries, revealing how parity and translation symmetries block-diagonalize the Liouvillian and enforce spectral equivalences.

(iii) Relaxation dynamics and NESS structure: we show

†Corresponding author. E-mail: zhangxz@tjnu.edu.cn

© 2026 Chinese Physical Society and IOP Publishing Ltd. All rights, including for text and data mining, AI training, and similar technologies, are reserved.

that multiple Liouvillian zero modes may arise, some of which are unphysical, and that the physically realized NESS is instead the unique linear combination determined by its overlap with the initial state.

Our main findings are as follows: (i) The Liouvillian gap exhibits a nonmonotonic dependence on dissipation strength, reaching a maximum at a finite value where the relaxation time is minimized. (ii) The position and sharpness of this maximum are governed by symmetry- and boundary-induced spectral transitions, such as those from purely imaginary to complex eigenvalues. This peak reflects an optimal interplay between coherent dynamics and dissipation, in which the system attains both the fastest relaxation and enhanced robustness against perturbations. By exploiting parity and rotational symmetries, we derive analytic expressions for the Liouvillian gap in both the weak-hopping and weak-dissipation regimes using non-Hermitian perturbation theory. These results provide design principles for optimizing relaxation times and stabilizing target nonequilibrium NESSs in quantum simulators, and shed light on the role of spectral singularities, symmetry, and finite-size effects in nonequilibrium quantum criticality.

2. General formalism

We begin our analysis with the Lindblad master equation,[19,20] derived under the Born–Markov approximation.[21] The time evolution of the density matrix ρ is governed by

$$\begin{aligned}\frac{\mathrm{d}\rho}{\mathrm{d}t} &= -\mathrm{i}[H,\rho]+\sum_{\alpha}\sum_{\{j\}}\left(L_{\alpha,j}\rho L_{\alpha,j}^{\dagger}-\frac{1}{2}\left\{L_{\alpha,j}^{\dagger}L_{\alpha,j},\rho\right\}\right)\\ &\equiv \mathcal{L}(\rho),\end{aligned} \tag{1}$$

where H denotes the system Hamiltonian, and $L_{\alpha,j}$ are the Lindblad jump operators. Here, the index α labels the type of dissipation, including dephasing (d) and asymmetric hopping to the right (R) or left (L), while j indexes the lattice sites on which these dissipative processes act independently before summation. The commutator $[A,B]=AB-BA$ and the anticommutator $\{A,B\}=AB+BA$ are used in the standard way. We set $\hbar\equiv 1$ throughout the paper. For computational convenience, we vectorize the density matrix ρ by stacking its columns into a single vector.[22] In this representation, a mixed-state density matrix $\rho=\sum_j p_j|\phi_j\rangle\langle\phi_j|$ is mapped to

$$\rho \longrightarrow \sum_j p_j|\phi_j\rangle\otimes|\phi_j\rangle. \tag{2}$$

Under this mapping, the Liouvillian superoperator $\mathcal{L}$ takes the form

$$\begin{aligned}\mathcal{L} &= \sum_{\alpha}\sum_{\{j\}}(L_{\alpha,j}^{*}\otimes L_{\alpha,j}-\frac{1}{2}I\otimes L_{\alpha,j}^{\dagger}L_{\alpha,j}-\frac{1}{2}L_{\alpha,j}^{\mathrm{T}}L_{\alpha,j}^{*}\otimes I)\\ &\quad -\mathrm{i}(I\otimes H-H^{\mathrm{T}}\otimes I).\end{aligned} \tag{3}$$

Assuming the system Hilbert space has dimension N, we promote the space of linear operators acting on it to a new Hilbert space of dimension N^2, endowed with the Hilbert–Schmidt inner product.[23] The Liouvillian eigenvalue problem is then defined as

$$\mathcal{L}(\rho_j^{\mathrm{R}})=\lambda_j\rho_j^{\mathrm{R}},\ \mathcal{L}^{\dagger}(\rho_j^{\mathrm{L}})=\lambda_j^{*}\rho_j^{\mathrm{L}},\ \ (j=0,1,\ldots,N^2-1), \tag{4}$$

where λ_j are the generally complex eigenvalues, and ρ_j^{R} and ρ_j^{L} are the corresponding right and left eigenmodes, forming a biorthonormal basis $\langle\rho_i^{\mathrm{L}}|\rho_j^{\mathrm{R}}\rangle=\delta_{i,j}$, with the completeness relation $\sum_j|\rho_j^{\mathrm{R}}\rangle\langle\rho_j^{\mathrm{L}}|=1$. The adjoint Liouvillian $\mathcal{L}^{\dagger}$ is given by

$$\begin{aligned}\mathcal{L}^{\dagger}(\rho) &= -\mathrm{i}[\rho,H]\\ &\quad +\sum_{\alpha}\sum_{\{j\}}\left(L_{\alpha,j}^{\dagger}\rho L_{\alpha,j}-\frac{1}{2}\left\{L_{\alpha,j}^{\dagger}L_{\alpha,j},\rho\right\}\right).\end{aligned} \tag{5}$$

Unlike the Hamiltonian of closed quantum systems, the spectrum of $\mathcal{L}$ typically contains complex eigenvalues.[22,24] The trace-preserving nature of the dynamics ensures that the real parts of all eigenvalues are non-positive, $\mathrm{Re}[\lambda_j]\leq 0$.[25,26] The unique NESS ρ_{ss} is defined as the right eigenvector corresponding to the zero eigenvalue[27]: $\mathcal{L}(\rho_{\mathrm{ss}})=0$. By sorting the eigenvalues in descending order of their real parts, we write

$$0=\mathrm{Re}[\lambda_0]\geqslant\mathrm{Re}[\lambda_1]\geqslant\mathrm{Re}[\lambda_2]\geqslant\cdots\geqslant\mathrm{Re}[\lambda_{N^2-1}], \tag{6}$$

and define the Liouvillian gap Δ[28] as

$$\Delta=|\mathrm{Re}[\lambda_1]|. \tag{7}$$

To investigate the interplay between dissipation and quantum coherence, we consider a noninteracting spinless fermion system governed by the Hamiltonian

$$H=-\sum_{\boldsymbol{r}}\sum_{\boldsymbol{\mu}=x,y,z}[t_{\boldsymbol{\mu}}c_{\boldsymbol{r}+\boldsymbol{\mu}}^{\dagger}c_{\boldsymbol{r}}+\mathrm{H.c.}]+\sum_{\boldsymbol{r}}V_{\boldsymbol{r}}c_{\boldsymbol{r}}^{\dagger}c_{\boldsymbol{r}}, \tag{8}$$

where $t_{\boldsymbol{\mu}}$ and $V_{\boldsymbol{r}}$ denote the nearest-neighbor hopping amplitude and the local potential, respectively. The fermionic creation and annihilation operators $c_{\boldsymbol{r}}^{\dagger}$ and $c_{\boldsymbol{r}}$ obey the standard anticommutation relations: $\{c_{\boldsymbol{r}}^{\dagger},c_{\boldsymbol{r}'}\}=\delta_{\boldsymbol{r}\boldsymbol{r}'}$, $\{c_{\boldsymbol{r}},c_{\boldsymbol{r}'}\}=\{c_{\boldsymbol{r}}^{\dagger},c_{\boldsymbol{r}'}^{\dagger}\}=0$. We consider three kinds of jump operators to model different dissipative processes: (i) $L_{\mathrm{d},\boldsymbol{r}}=\sqrt{\gamma_{\mathrm{d}}}c_{\boldsymbol{r}}^{\dagger}c_{\boldsymbol{r}}$[29] (dephasing); (ii) $L_{\mathrm{R},\boldsymbol{r}}=\sqrt{\gamma_{\mathrm{R}}}c_{\boldsymbol{r}+\boldsymbol{\mu}}^{\dagger}c_{\boldsymbol{r}}$ (rightward hopping); (iii) $L_{\mathrm{L},\boldsymbol{r}}=\sqrt{\gamma_{\mathrm{L}}}c_{\boldsymbol{r}-\boldsymbol{\mu}}^{\dagger}c_{\boldsymbol{r}}$[30] (leftward hopping). Here, γ_{d}, γ_{R}, and γ_{L} denote the rates of dephasing, rightward hopping, and leftward hopping, respectively. The operators $L_{\mathrm{d},\boldsymbol{r}}$ represent on-site dephasing, while $L_{\mathrm{R},\boldsymbol{r}}$ and $L_{\mathrm{L},\boldsymbol{r}}$ induce asymmetric incoherent hopping to adjacent sites. In the following sections, we categorize these jump operators into two classes: local dephasing ($\alpha=\mathrm{d}$) and directional hopping ($\alpha=\mathrm{R},\mathrm{L}$). We then examine their respective influences under both open boundary conditions (OBC) and periodic boundary conditions (PBC).

3. Type I: dephasing model ($\alpha = \mathrm{d}$)

We now consider a specific one-dimensional lattice system to explore its NESS and Liouvillian spectral gap. The Hamiltonian is given by

$$H = -t\sum_j c_j^\dagger c_{j+1} + \mathrm{H.c.}, \tag{9}$$

where t is the nearest-neighbor hopping amplitude. For simplicity, we neglect any on-site potential. The lattice with open boundary conditions naturally exhibits spatial inversion symmetry about its center. To analyze the system's symmetries, we define the parity operator P satisfying $P^2 = I$, $P^\dagger = P^{-1} = P$, where I is the identity operator. Its action on fermionic creation operators is given by $Pc_j^\dagger P^{-1} = c_{N+1-j}^\dagger$.[31] Similarly, on single-particle basis states, $P|\varphi_{0,j}\rangle = |\varphi_{0,N+1-j}\rangle$, where N is assumed to be an odd number for simplicity. The ket $|\varphi_{0,j}\rangle = c_j^\dagger|0\rangle$ denotes a single-particle state localized at site j, with $|0\rangle$ being the vacuum state. Applying P to the Hamiltonian yields $PHP^{-1} = H$, indicating that the Hamiltonian is invariant under spatial inversion and thus possesses parity symmetry. We next examine whether the Liouvillian retains parity symmetry under a specific dissipative process. Consider the Lindblad jump operator $L_{\mathrm{d},j} = \sqrt{\gamma_\mathrm{d}} c_j^\dagger c_j$ acting only at the middle site of the system, $j = (N+1)/2$, and denote the corresponding Liouvillian as $\mathcal{L}_{(N+1)/2}$. From the parity transformation, we find

$$[P, L_{\mathrm{d},(N+1)/2}] = 0, \tag{10}$$

$$[P, L_{\mathrm{d},(N+1)/2}^\dagger L_{\mathrm{d},(N+1)/2}] = 0, \tag{11}$$

$$[P, L_{\mathrm{d},(N+1)/2}^\mathrm{T} L_{\mathrm{d},(N+1)/2}^*] = 0. \tag{12}$$

We now consider the action of the parity transformation on the vectorized Liouvillian in Liouville space. For example,

$$\begin{aligned} I\otimes H &= (PIP^{-1})\otimes(PHP^{-1}) \\ &= (P\otimes P)(I\otimes H)(P^{-1}\otimes P^{-1}), \end{aligned} \tag{13}$$

$$\begin{aligned} L_{\mathrm{d},(N+1)/2}^*\otimes L_{\mathrm{d},(N+1)/2} &= (P\otimes P)(L_{\mathrm{d},(N+1)/2}^*\otimes L_{\mathrm{d},(N+1)/2}) \\ &\quad\times(P^{-1}\otimes P^{-1}), \end{aligned} \tag{14}$$

$$\begin{aligned} I\otimes L_{\mathrm{d},(N+1)/2}^\dagger L_{\mathrm{d},(N+1)/2} &= (P\otimes P)(I\otimes L_{\mathrm{d},(N+1)/2}^\dagger L_{\mathrm{d},(N+1)/2}) \\ &\quad\times(P^{-1}\otimes P^{-1}). \end{aligned} \tag{15}$$

Therefore, the full Liouvillian obeys the transformation rule

$$(P\otimes P)\mathcal{L}_{(N+1)/2}(P^{-1}\otimes P^{-1}) = \mathcal{L}_{(N+1)/2}, \tag{16}$$

which motivates the definition of an extended parity operator in Liouville space, $\mathcal{P} = P\otimes P$, with $\mathcal{P}^{-1} = P^{-1}\otimes P^{-1}$. The Liouvillian $\mathcal{L}_{(N+1)/2}$ thus satisfies $[\mathcal{P}, \mathcal{L}_{(N+1)/2}] = 0$, confirming that it preserves parity symmetry under this specific dissipative configuration. On the other hand, the action of $\mathcal{P}$ on the density matrix ρ is given by

$$\begin{aligned} \mathcal{P}\rho &= \sum_{j,k}\rho_{jk} P|\varphi_{0,j}\rangle\langle\varphi_{0,k}|P^{-1} \\ &= \sum_{j,k}\rho_{N+1-j,N+1-k}|\varphi_{0,j}\rangle\langle\varphi_{0,k}|. \end{aligned} \tag{17}$$

That is, the matrix elements of ρ are reflected about the center of the chain.

3.1. The case of $\mathcal{L}_2$

For a concrete example with a three-site chain, the parity transformation corresponds to

$$\mathcal{P}\rho = \mathcal{P}\begin{pmatrix}\rho_{11}\\ \rho_{21}\\ \rho_{31}\\ \rho_{12}\\ \rho_{22}\\ \rho_{32}\\ \rho_{13}\\ \rho_{23}\\ \rho_{33}\end{pmatrix} = \begin{pmatrix}\rho_{33}\\ \rho_{23}\\ \rho_{13}\\ \rho_{32}\\ \rho_{22}\\ \rho_{12}\\ \rho_{31}\\ \rho_{21}\\ \rho_{11}\end{pmatrix}, \tag{18}$$

which corresponds to a spatial inversion of the density matrix about its central element ρ_{22}

$$\mathcal{P}\rho = P\rho P = \begin{pmatrix}\rho_{33} & \rho_{32} & \rho_{31}\\ \rho_{23} & \rho_{22} & \rho_{21}\\ \rho_{13} & \rho_{12} & \rho_{11}\end{pmatrix}. \tag{19}$$

Thus, parity acts on the density matrix as a mirror reflection with respect to the central site, while preserving Hermiticity and the trace.

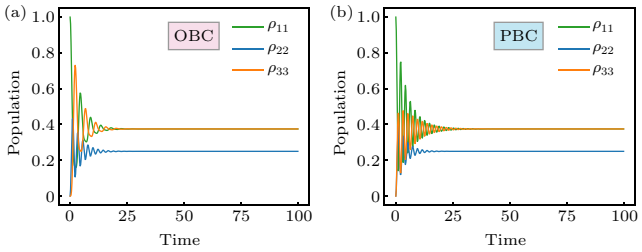


Fig. 1. Time evolution of the particle number densities ρ_{11}, ρ_{22}, and ρ_{33} under (a) OBC and (b) PBC, with system parameters $N = 3$, $t = 1$, and $\gamma_d = 1$. Under PBC, the oscillation frequencies of ρ_{11} and ρ_{33} are significantly higher than under OBC and are also much more pronounced than those of ρ_{22}. The oscillation amplitude of ρ_{22} shows little difference between OBC and PBC. Regarding the relaxation dynamics, all three densities relax at nearly the same rate under OBC, whereas under PBC, ρ_{11} and ρ_{33} exhibit markedly slower relaxation than ρ_{22}, which reaches the NESS more quickly. In the long-time limit, both ρ_{11} and ρ_{33} converge to the same NESS value, which exceeds that of ρ_{22}, indicating a NESS particle distribution favoring the boundary sites.

We initialize the chain in $\rho_{\mathrm{ini},1} = |\varphi_{0,1}\rangle\langle\varphi_{0,1}|$ and numerically integrate the master equation $d\rho/dt = \mathcal{L}_2\rho$ under both open (OBC) and periodic (PBC) boundary conditions. Figure 1 plots the time evolution of site densities $\rho_{jj}(t) = \mathrm{Tr}[\rho(t)c_j^\dagger c_j]$ for OBC (solid) and PBC (dashed). Although small transients differ, both cases relax to the same long-time

profile. We also find two zero-eigenvalue right modes, $\rho_{\rm ss}^{(1)}$ and $\rho_{\rm ss}^{(2)}$. Under OBC, their normalized matrix forms are

$$\rho_{\rm (O)ss}^{(1)} = \begin{pmatrix} 0.375 & 0 & -0.125 \\ 0 & 0.25 & 0 \\ -0.125 & 0 & 0.375 \end{pmatrix},$$
$$\rho_{\rm (O)ss}^{(2)} = \begin{pmatrix} 0 & 0 & 1 \\ 0 & 1 & 0 \\ 1 & 0 & 0 \end{pmatrix}. \quad (20)$$

The purity of $\rho_{\rm (O)ss}^{(1)}$ is found to be $\mathrm{Tr}[(\rho_{\rm (O)ss}^{(1)})^2] = 0.375 < 1$, indicating that it represents a mixed state. In contrast, $\rho_{\rm (O)ss}^{(2)}$ yields a purity of $\mathrm{Tr}[(\rho_{\rm (O)ss}^{(2)})^2] = 3 > 1$, which violates the physical requirement for density matrices. Hence, $\rho_{\rm (O)ss}^{(2)}$ is unphysical. However, since the initial state has zero overlap with this eigenstate (i.e., the projection coefficient $b_1 = 0$), it does not contribute to the dynamics. Consequently, the NESS of the system is solely determined by $\rho_{\rm (O)ss}^{(1)}$

$$\rho_{\rm ss(O)} = a_1\rho_{\rm (O)ss}^{(1)} + b_1\rho_{\rm (O)ss}^{(2)} = \rho_{\rm (O)ss}^{(1)}. \quad (21)$$

A similar analysis is performed under PBC, where two zero-eigenvalue modes of the Liouvillian are found

$$\rho_{\rm (P)ss}^{(1)} = \begin{pmatrix} 0.297+0.062\mathrm{i} & 0 & 0.110-0.186\mathrm{i} \\ 0 & 0.406-0.124\mathrm{i} & 0 \\ 0.110-0.186\mathrm{i} & 0 & 0.297+0.062\mathrm{i} \end{pmatrix}, \quad (22)$$

$$\rho_{\rm (P)ss}^{(2)} = \begin{pmatrix} 0.219-0.197\mathrm{i} & 0 & 0.342+0.590\mathrm{i} \\ 0 & 0.562+0.393\mathrm{i} & 0 \\ 0.342+0.590\mathrm{i} & 0 & 0.219-0.197\mathrm{i} \end{pmatrix}. \quad (23)$$

Due to the degeneracy, the purities of $\rho_{\rm (P)ss}^{(1)}$ and $\rho_{\rm (P)ss}^{(2)}$ are found to be complex numbers, thus violating physicality. However, the projections of the initial state onto these two zero modes yield nonzero complex coefficients

$$a_2 = 0.49041 - 0.3929\mathrm{i},$$
$$b_2 = -0.10599 + 0.45147\mathrm{i}, \quad (24)$$

indicating that the unphysical eigenvectors $\rho_{\rm (P)ss}^{(1)}$ and $\rho_{\rm (P)ss}^{(2)}$, although not valid density matrices on their own, contribute to the NESS dynamics. The NESS of the system is then given by

$$\rho_{\rm ss(P)} = a_2\rho_{\rm (P)ss}^{(1)} + b_2\rho_{\rm (P)ss}^{(2)} = \begin{pmatrix} 0.375 & 0 & -0.125 \\ 0 & 0.25 & 0 \\ -0.125 & 0 & 0.375 \end{pmatrix}, \quad (25)$$

which is a valid, Hermitian, and positive semi-definite mixed state. This analysis demonstrates that, under both boundary conditions, the NESS is not uniquely determined by the spectrum of the Liouvillian alone, but also depends sensitively on the choice of the initial state. In the following, we present an example that further illustrates this dependence.

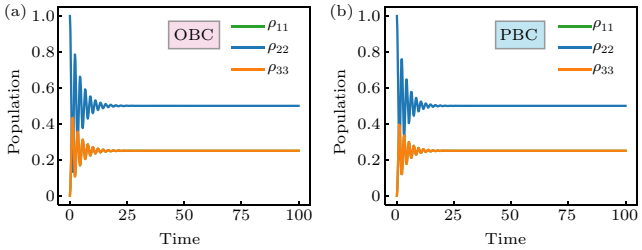


Fig. 2. Time evolution of the particle number densities ρ_{11}, ρ_{22}, and ρ_{33} under (a) OBC and (b) PBC, with parameters $N = 3$, $t = 1$, and $\gamma_{\rm d} = 1$. A prominent feature in both cases is that the curves for ρ_{11} and ρ_{33} overlap exactly over the entire time interval. The oscillation amplitudes of ρ_{11}, ρ_{22}, and ρ_{33} are of comparable magnitude, although the oscillation ranges of ρ_{11} and ρ_{33} overlap only partially with that of ρ_{22}. Regarding relaxation behavior, all three densities reach their NESSs at approximately the same time. In the long-time limit, ρ_{11} and ρ_{33} converge to equal values, both lower than that of ρ_{22}, forming a spatial distribution in which the central site hosts a higher particle density than the edges.

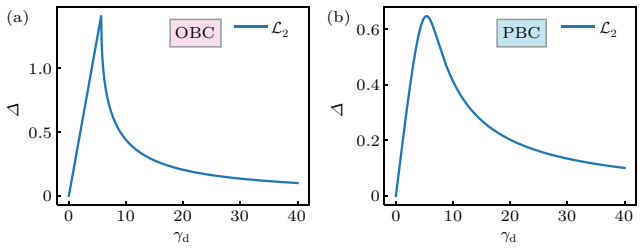


Fig. 3. Liouvillian gap Δ as a function of the dissipation rate $\gamma_{\rm d}$ under (a) OBC and (b) PBC. The system parameters are fixed as $N = 3$, $t = 1$, and $\gamma_{\rm d} \in [0, 40]$. In both cases, the peak in Δ occurs within the range $\gamma_{\rm d} \in [5, 10]$, marking a significant turning point in the spectral behavior. However, the peak magnitude of Δ under OBC is larger than that under PBC. Additionally, the shape of the peak under OBC is significantly sharper, with steeper slopes on both sides, while the PBC case shows a more gradual variation. This contrast suggests a more pronounced spectral response to dissipation under OBC.

We now consider a different initial state $\rho_{\rm ini,2} = |\varphi_{0,2}\rangle\langle\varphi_{0,2}|$ and examine the corresponding time evolution, as shown in Fig. 2. Compared to the dynamics initialized from $\rho_{\rm ini,1} = |\varphi_{0,1}\rangle\langle\varphi_{0,1}|$, the numerical results reveal that the system relaxes to distinct NESSs

$$\rho_{ss(\rm OBC)} = \rho_{ss(\rm PBC)} = \begin{pmatrix} 0.25 & 0 & 0.25 \\ 0 & 0.5 & 0 \\ 0.25 & 0 & 0.25 \end{pmatrix}. \quad (26)$$

Next, we proceed to analyze the Liouvillian gap Δ under both OBC and PBC. Figure 3 presents the behavior of the gap as a function of the dephasing rate $\gamma_{\rm d}$. In both cases, the Liouvillian gap exhibits a nonmonotonic dependence on $\gamma_{\rm d}$: it initially increases, reaches a peak, and then decreases as $\gamma_{\rm d}$ continues to grow. Notably, the peak under OBC is sharper than that under PBC. Since the Liouvillian in both boundary conditions respects parity symmetry, we can exploit this symmetry to block-diagonalize the Liouvillian and obtain analytical insights into its spectrum. To proceed, we define the single-site basis states

$$|\varphi_{0,1}\rangle = \begin{pmatrix} 1 \\ 0 \\ 0 \end{pmatrix}, \ |\varphi_{0,2}\rangle = \begin{pmatrix} 0 \\ 1 \\ 0 \end{pmatrix}, \ |\varphi_{0,3}\rangle = \begin{pmatrix} 0 \\ 0 \\ 1 \end{pmatrix}. \quad (27)$$

The parity operator P, defined to swap the outer two sites about the center, takes the following matrix form in the site basis

$$P = \begin{pmatrix} 0 & 0 & 1 \\ 0 & 1 & 0 \\ 1 & 0 & 0 \end{pmatrix}, \tag{28}$$

and the corresponding $\mathcal{P}$ superoperator is given by $\mathcal{P} = P \otimes P$. The Liouvillian $\mathcal{L}_2$ commutes with the parity operator, $[\mathcal{L}_2, \mathcal{P}] = 0$, and can thus be block-diagonalized in the eigenbasis of $\mathcal{P}$. The eigenvalues of $\mathcal{P}$ are ± 1, and the corresponding eigenvectors form the following basis:

(i) Parity -1 subspace

$$\begin{bmatrix} 0 \\ 0 \\ 0 \\ -1 \\ 0 \\ 1 \\ 0 \\ 0 \\ 0 \end{bmatrix}, \begin{bmatrix} 0 \\ 0 \\ -1 \\ 0 \\ 0 \\ 0 \\ 1 \\ 0 \\ 0 \end{bmatrix}, \begin{bmatrix} 0 \\ -1 \\ 0 \\ 0 \\ 0 \\ 0 \\ 0 \\ 1 \\ 0 \end{bmatrix}, \begin{bmatrix} -1 \\ 0 \\ 0 \\ 0 \\ 0 \\ 0 \\ 0 \\ 0 \\ 1 \end{bmatrix}; \text{(4-dimensional)}. \tag{29}$$

(ii) Parity $+1$ subspace

$$\begin{bmatrix} 0 \\ 0 \\ 0 \\ 0 \\ 1 \\ 0 \\ 0 \\ 0 \\ 0 \end{bmatrix}, \begin{bmatrix} 0 \\ 0 \\ 0 \\ 1 \\ 0 \\ 1 \\ 0 \\ 0 \\ 0 \end{bmatrix}, \begin{bmatrix} 0 \\ 0 \\ 1 \\ 0 \\ 0 \\ 0 \\ 1 \\ 0 \\ 0 \end{bmatrix}, \begin{bmatrix} 0 \\ 1 \\ 0 \\ 0 \\ 0 \\ 0 \\ 0 \\ 1 \\ 0 \end{bmatrix}, \begin{bmatrix} 1 \\ 0 \\ 0 \\ 0 \\ 0 \\ 0 \\ 0 \\ 0 \\ 1 \end{bmatrix}; \text{(5-dimensional)}. \tag{30}$$

The Liouvillian thus decomposes into two invariant subspaces of dimensions 4×4 and 5×5, respectively. In the OBC case, the NESS is found in the parity $+1$ (5-dimensional) subspace. We then focus on the parity -1 (4-dimensional) subspace to determine the first excited state, obtaining the following analytical expression for the Liouvillian gap Δ:

$$\Delta_{(\mathrm{OBC})} = \left| \mathrm{Re}\left[\sqrt{\frac{1}{16}\gamma_\mathrm{d}^2 - 2t^2} - \frac{1}{4}\gamma_\mathrm{d} \right] \right|. \tag{31}$$

For the PBC case, a similar block-diagonalization yields the NESS in the 5×5 subspace and the first excited state in the 4×4 subspace, with Liouvillian gap Δ:

$$\Delta_{(\mathrm{PBC})} = \left| \mathrm{Re}\left[-\frac{1}{4}\gamma_\mathrm{d} + \mathrm{i}\sqrt{\frac{9}{4}t^2 - \frac{1}{4}\mathrm{i}t\gamma_\mathrm{d} - \frac{1}{16}\gamma_\mathrm{d}^2} \right] \right|. \tag{32}$$

From the above expressions, we can understand the origin of the peak structure in the Δ–γ_d curves. In the OBC case, the appearance of a peak is due to a transition from purely imaginary to complex eigenvalues. Before this transition point, the real part of the eigenvalue is given by a linear function $\frac{1}{4}\gamma_\mathrm{d}$, independent of t, leading to a linearly increasing gap. Numerically, the peak occurs at $\gamma_{\mathrm{d}(\mathrm{OBC})} = 5.6528$, with $\Delta_{(\mathrm{OBC})} = 1.4107$. In contrast, for the PBC case, the peak in the gap arises from a change in the slope of the real part of the eigenvalue. Here, the transition is smoother, and the peak is reached at $\gamma_{\mathrm{d}(\mathrm{PBC})} = 5.3627$, with $\Delta_{(\mathrm{PBC})} = 0.6470$.

At the same time, this reveals a possible underlying competition mechanism in the system. Specifically, in the weak dissipation regime, where γ_d is small, the system dynamics are predominantly governed by the coherent Hamiltonian H. Here, the environment causes a slow "leakage" of information but is insufficient to rapidly correct deviations induced by coherent evolution. As γ_d increases, dissipation accelerates and the system is driven back to the steady state more efficiently, leading to a growth of the Liouvillian gap and a corresponding decrease of the relaxation time. When γ_d reaches an optimal value, corresponding to the peak of the gap, the dissipation rate precisely compensates for errors accumulated through coherent evolution. At this point, dissipation and coherent dynamics achieve an optimal balance, yielding maximal robustness against perturbations. This manifests as the largest Liouvillian gap and the shortest relaxation time. Beyond this optimal dissipation strength, the system enters a strong-dissipation regime. Frequent interactions with the environment strongly suppress coherent evolution, causing perturbations away from the target steady state to relax more slowly. Consequently, the Liouvillian gap decreases and the relaxation time increases with further growth of γ_d. This difference in peak sharpness reflects the distinct spectral structures under different boundary conditions.

3.2. The case of $\mathcal{L}_1$ and $\mathcal{L}_3$

We investigate the time evolution governed by the master equation $\mathrm{d}\rho/\mathrm{d}t = \mathcal{L}_1\rho$, where the jump operator is applied only at site $j = 1$. The system is initialized in the pure state $\rho_{\mathrm{ini},1} = |\varphi_{0,1}\rangle\langle\varphi_{0,1}|$, and we numerically solve the dynamics under both OBC and PBC, as illustrated in Fig. 4. In this configuration, the behavior of the NESS differs markedly from that under the Liouvillian $\mathcal{L}_2$. Specifically, under $\mathcal{L}_1$, we observe that the NESS under OBC is unique and independent of the initial condition, while under PBC, the NESS is generally not unique and depends sensitively on the choice of initial state. Under OBC, we find that the system relaxes to the maximally mixed state, $\rho_\mathrm{ss} = I/3$, in which the probability of occupation is uniformly distributed among all three lattice sites. The corresponding purity is $1/3$, corresponding to a totally mixed state. Due to the underlying parity symmetry of the system, the dissipators satisfy the following relations:

$$PL_{\mathrm{d},1}P^{-1} = L_{\mathrm{d},3}, \tag{33}$$

$$P(L_{\mathrm{d},1}^\dagger L_{\mathrm{d},1})P^{-1} = L_{\mathrm{d},3}^\dagger L_{\mathrm{d},3}, \tag{34}$$

$$P(L_{\mathrm{d},1}^\mathrm{T} L_{\mathrm{d},1}^*)P^{-1} = L_{\mathrm{d},3}^\mathrm{T} L_{\mathrm{d},3}^*. \tag{35}$$

These relations imply that the Liouvillians $\mathcal{L}_1$ and $\mathcal{L}_3$ are connected by a parity transformation $\mathcal{P}\mathcal{L}_1\mathcal{P}^{-1} = \mathcal{L}_3$. Let $\rho_{\mathrm{ss},1}$ and $\rho_{\mathrm{ss},3}$ denote the NESSs of $\mathcal{L}_1$ and $\mathcal{L}_3$, respectively. It then follows that $\mathcal{P}\rho_{\mathrm{ss},1} = \rho_{\mathrm{ss},3}$. This demonstrates that under OBC, the NESSs of the systems with localized dissipation at sites 1 and 3 are related by parity, and in fact coincide in the case of a maximally mixed state. However, under PBC, this symmetry no longer guarantees identical NESSs. The presence of multiple zero modes in the Liouvillian spectrum under PBC leads to a dependence of the NESS on the initial condition, and the parity relation between $\mathcal{L}_1$ and $\mathcal{L}_3$ does not necessarily extend to their NESSs. To investigate the dependence of the NESS on the initial condition, we numerically solved the dynamics generated by $\mathcal{L}_1$ with three different initial states: $\rho_{\mathrm{ini},1} = |\varphi_{0,1}\rangle\langle\varphi_{0,1}|$, $\rho_{\mathrm{ini},2} = |\varphi_{0,2}\rangle\langle\varphi_{0,2}|$, and $\rho_{\mathrm{ini},3} = |\varphi_{0,3}\rangle\langle\varphi_{0,3}|$. The corresponding NESSs are found to be

$$\rho_{\mathrm{ss},1} = \begin{pmatrix} 0.5 & 0 & 0 \\ 0 & 0.25 & 0.25 \\ 0 & 0.25 & 0.25 \end{pmatrix}, \quad \rho'_{\mathrm{ss},1} = \rho''_{\mathrm{ss},1},$$
$$\rho'_{\mathrm{ss},1} = \begin{pmatrix} 0.25 & 0 & 0 \\ 0 & 0.375 & -0.125 \\ 0 & -0.125 & 0.375 \end{pmatrix}. \tag{36}$$

Similarly, for $\mathcal{L}_3$ under PBC, the NESSs corresponding to the same three initial conditions are

$$\rho_{\mathrm{ss},3} = \begin{pmatrix} 0.375 & -0.125 & 0 \\ -0.125 & 0.375 & 0 \\ 0 & 0 & 0.25 \end{pmatrix}, \quad \rho'_{\mathrm{ss},3} = \rho_{\mathrm{ss},3},$$
$$\rho''_{\mathrm{ss},3} = \begin{pmatrix} 0.25 & 0.25 & 0 \\ 0.25 & 0.25 & 0 \\ 0 & 0 & 0.5 \end{pmatrix}. \tag{37}$$

These results reveal a classification of the NESSs into two distinct types, depending on whether the initial position of the particle coincides with the location of the dissipative jump operator. When the initial state is $\rho_{\mathrm{ini},1}$ or $\rho_{\mathrm{ini},3}$, the NESSs of $\mathcal{L}_1$ and $\mathcal{L}_3$ exhibit different spatial structures. In contrast, when the initial state is $\rho_{\mathrm{ini},2}$, the NESSs are related by a parity transformation. Specifically, denoting the parity operator in the nine-dimensional Liouville space as $\mathcal{P}$, one has $\mathcal{P}\rho'_{\mathrm{ss},1} = \rho'_{\mathrm{ss},3}$. This observation highlights the conditional relevance of symmetry relations under PBC: although the Liouvillians $\mathcal{L}_1$ and $\mathcal{L}_3$ are related by a parity transformation, their NESSs only obey this symmetry when the initial condition is itself symmetric with respect to the jump location.

We now turn to an analysis of the Δ–γ_{d} dependence of the Liouvillians $\mathcal{L}_1$ and $\mathcal{L}_3$, shown in Fig. 5 under both OBC and PBC. Due to the parity symmetry relation $\mathcal{P}\mathcal{L}_1\mathcal{P}^{-1} = \mathcal{L}_3$, the curves for $\mathcal{L}_1$ and $\mathcal{L}_3$ coincide exactly, regardless of the boundary condition. In both OBC and PBC cases, the spectral gap Δ exhibits a characteristic non-monotonic behavior with increasing γ_{d}, first increasing and then decreasing, similar to what we previously observed for $\mathcal{L}_2$. This implies the existence of a peak in the spectral gap as a function of dissipation strength. Moreover, from a dynamical perspective, the peak thus corresponds to an optimal dissipation strength at which the slowest relaxation mode is accelerated to the greatest extent and the overall relaxation time is minimized. Simultaneously, this peak indicates maximal system resilience to disturbances, enabling the fastest relaxation from initial states to the steady state. This highlights the beneficial role of properly tuned dissipation in optimizing quantum system dynamics. Under OBC, the absence of translation or parity symmetry renders an exact analytical solution of the Liouvillian spectrum intractable.

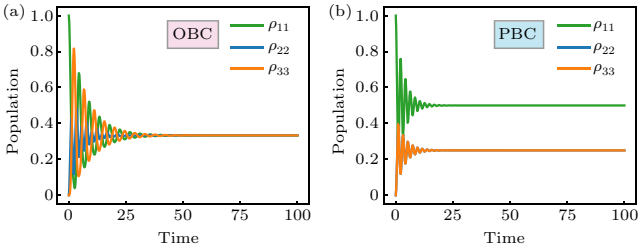


Fig. 4. Time evolution of particle number densities ρ_{11}, ρ_{22}, and ρ_{33} under (a) OBC and (b) PBC, with system parameters $N = 3$, $t = 1$, and $\gamma_{\mathrm{d}} = 1$. The oscillatory behavior exhibits clear differences between OBC and PBC. Under OBC, although the curves for ρ_{11}, ρ_{22}, and ρ_{33} do not overlap, all three densities oscillate within a similar amplitude range throughout the relaxation process. In contrast, under PBC, the curves of ρ_{22} and ρ_{33} are identical and overlap with ρ_{11} only briefly at the beginning of the evolution. In terms of relaxation time, the system under OBC exhibits a significantly longer relaxation time compared to that under PBC, indicating that the PBC system reaches a NESS earlier. At long times, the NESS distribution under OBC becomes uniform with $\rho_{11} = \rho_{22} = \rho_{33} = 1/3$, while under PBC, $\rho_{22} = \rho_{33} < \rho_{11}$, indicating an asymmetric NESS particle distribution favoring site 1.

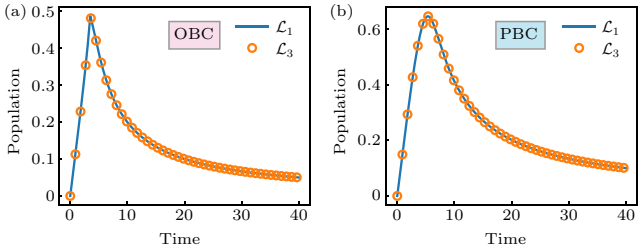


Fig. 5. Liouvillian gap Δ associated with the Liouvillian operators $\mathcal{L}_1$ and $\mathcal{L}_3$ under (a) OBC and (b) PBC, with parameters $N = 3$, $t = 1$, and $\gamma_{\mathrm{d}} \in [0, 40]$. The curves for $\mathcal{L}_1$ and $\mathcal{L}_3$ overlap exactly under both boundary conditions. As γ_{d} increases, the peak of the Liouvillian gap appears at a lower γ_{d} in the OBC case compared to the PBC case. However, the peak height is larger under PBC than under OBC. In terms of shape, both peaks exhibit slope changes on either side, but the peak under OBC is notably sharper, while the peak under PBC is smoother.

Nevertheless, our numerical investigation indicates that the peak in Δ persists even when the tunneling amplitude t or the dissipation rate γ_{d} is small. Motivated by this observation, we treat t and γ_{d} as small perturbative parameters and employ perturbation theory[32,33] to approximate the Liouvillian eigenvalues. This approach allows us to qualitatively reproduce the rise-and-fall structure of the Δ–γ_{d} curve and to

gain insight into the underlying physical mechanisms driving the spectral behavior.

Using these perturbative methods, we plotted two intersecting dashed lines in Fig. 6 to approximate the rise-and-fall behavior of the spectral gap Δ as a function of γ_d for the Liouvillian $\mathcal{L}_1$. The results show that in the regimes where either t or γ_d is small, the perturbative predictions agree well with the exact numerical calculations. However, as the parameters approach the region near the peak, the perturbative approximation gradually breaks down. At the peak itself, the numerically obtained maxima are marked with distinct colored "+" symbols to emphasize the discrepancies between different peak values. A detailed derivation of the perturbative results is provided in Appendix A.

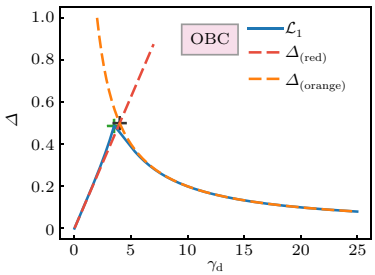


Fig. 6. Comparison between the approximate and numerical solutions for the Liouvillian gap Δ as a function of the dissipation rate γ_d under OBC. The red and orange dashed curves represent the perturbative approximations, while the blue solid curve shows the exact numerical solution. The system parameters are $N = 3$, $t = 1$, and $\gamma_d \in [0, 25]$. The green and black "+" symbols indicate the peak positions obtained from the numerical and approximate results, respectively. Specifically, the peak values are $(\gamma_d^{(\text{green})}, \Delta^{(\text{green})}) = (3.5043, 0.4864)$ and $(\gamma_d^{(\text{black})}, \Delta^{(\text{black})}) = (4, 0.5)$. The close agreement between the approximate and exact solutions across a wide range of γ_d provides strong evidence for the validity of the perturbative approach. Furthermore, the successful reproduction of the increasing and decreasing behavior of Δ in both the small and large γ_d regimes helps to clarify the physical origin and inevitability of the peak structure in the Liouvillian spectrum of $\mathcal{L}_1$.

Before ending this part, we emphasize that under PBC, the Δ–γ_d curves for $\mathcal{L}_1$, $\mathcal{L}_2$, and $\mathcal{L}_3$ coincide due to the system's rotational (i.e., translational) symmetry.[34,35] This symmetry ensures that all three Liouvillian operators are related by a unitary transformation, leading to identical spectra and, consequently, the same Liouvillian gap. To make this explicit, we define the rotation operator R, which acts on fermionic creation operators as $Rc_j^\dagger R^{-1} = c_{j+k}^\dagger$, and similarly on the single-particle states: $R|\varphi_{0,j}\rangle = |\varphi_{0,j+k}\rangle$. For simplicity, we consider the case $N = 3$ and take $k = 1$. Applying R to the dissipative jump operators, we obtain

$$RL_{d,1}R^{-1} = R(\sqrt{\gamma_d}c_1^\dagger c_1)R^{-1} = \sqrt{\gamma_d}c_2^\dagger c_2 = L_{d,2}, \quad (38)$$

$$RL_{d,2}R^{-1} = L_{d,3}, \quad (39)$$

$$RL_{d,3}R^{-1} = L_{d,1}. \quad (40)$$

Extending this to the Liouvillian level, we define the rotation superoperator as $\mathcal{R} = R \otimes R$ with $\mathcal{R}^{-1} = R^{-1} \otimes R^{-1}$. The Liouvillian operators then transform cyclically under

$$\mathcal{R}\mathcal{L}_1\mathcal{R}^{-1} = \mathcal{L}_2, \quad (41)$$

$$\mathcal{R}\mathcal{L}_2\mathcal{R}^{-1} = \mathcal{L}_3, \quad (42)$$

$$\mathcal{R}\mathcal{L}_3\mathcal{R}^{-1} = \mathcal{L}_1. \quad (43)$$

This establishes that $\mathcal{L}_1$, $\mathcal{L}_2$, and $\mathcal{L}_3$ are unitarily equivalent under rotation. Consequently, their NESSs are related by the rotation symmetry, and they share identical Liouvillian spectra and gaps.

3.3. The case of $\mathcal{L}_{123}$

We now extend our analysis by modifying the position and number of quantum jump operators such that the set $\{j\}$ spans all lattice sites. Numerically solving the evolution of the system governed by $\mathrm{d}\rho/\mathrm{d}t = \mathcal{L}_{123}\rho$ from the initial state $\rho_{\text{ini},1} = |\varphi_{0,1}\rangle\langle\varphi_{0,1}|$, we present the results in Fig. 7. It is observed that, in this fully dissipative case, both the OBC and PBC boundary systems converge to the same unique NESS, which coincides with that of $\mathcal{L}_1$: the maximally mixed state $\rho_{ss} = I/3$. The condition for the NESS to be the identity matrix can be derived directly from the structure of the Liouvillian. If the NESS is $\rho_{ss} = I/3$, then the following condition must hold:

$$\sum_\alpha \sum_{\{j\}} \left(L_{\alpha,j}\rho L_{\alpha,j}^\dagger - \frac{1}{2}\{L_{\alpha,j}^\dagger L_{\alpha,j}, \rho\} \right) = 0, \quad -\mathrm{i}[H, I] = 0.$$

This implies that a necessary and sufficient condition for the identity matrix to be a NESS is

$$[L_{\alpha,j}, L_{\alpha,j}^\dagger] = 0. \quad (44)$$

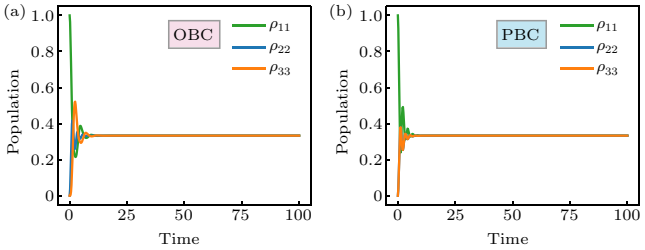


Fig. 7. Time evolution of particle number densities ρ_{11}, ρ_{22}, and ρ_{33} under (a) OBC and (b) PBC, with system parameters $N = 3$, $t = 1$, and $\gamma_d = 1$. The oscillation amplitudes and frequencies of all three densities are comparable under both OBC and PBC, and the oscillations largely occur within similar amplitude ranges. In both boundary conditions, the relaxation times of ρ_{11}, ρ_{22}, and ρ_{33} are very short, with the system reaching its NESS after only a few rapid oscillations. At long times, the NESS distribution is uniform across all three sites, with $\rho_{11} = \rho_{22} = \rho_{33} = 1/3$ under both OBC and PBC.

We next focus on the behavior of the Liouvillian gap Δ under this fully dissipative setting (Fig. 8). As in previous cases, Δ exhibits a peak as a function of γ_d, indicating a trade-off between dissipation and coherent dynamics. Notably, under OBC, the peak value of Δ matches that found in the $\mathcal{L}_2$ scenario, while under PBC, the peak becomes sharper compared to the single-jump-operator case. Using symmetry considerations, we obtain analytic expressions for the first excited

eigenvalue of the Liouvillian and hence for the Liouvillian gap in both boundary conditions. For OBC, straightforward algebra shows

$$\Delta_{(\mathrm{OBC})} = \left| \mathrm{Re}\left[\sqrt{\frac{1}{4}\gamma_\mathrm{d}^2 - 2t^2} - \frac{1}{2}\gamma_\mathrm{d} \right] \right|. \tag{45}$$

For PBC, the exact results are

$$\Delta_{(\mathrm{PBC})} = \left| \mathrm{Re}\left[\Lambda - \frac{3t^2 - \frac{1}{9}\gamma_\mathrm{d}^2}{\Lambda} - \frac{2}{3}\gamma_\mathrm{d} \right] \right|, \tag{46}$$

where

$$\Lambda = \sqrt[3]{\frac{\gamma_\mathrm{d}^3}{27} + \sqrt{27t^6 - 3t^4\gamma_\mathrm{d}^2 + \frac{1}{9}t^2\gamma_\mathrm{d}^4}}. \tag{47}$$

From these analytic expressions, we see that in the OBC case, the peak in $\Delta_{(\mathrm{OBC})}$ originates from a transition in the eigenvalue λ_1 from purely imaginary to complex, consistent with earlier analyses. Numerically, this transition occurs at $\gamma_{\mathrm{d}(\mathrm{OBC})} = 2.8214$, yielding a peak value $\Delta_{(\mathrm{OBC})} = 1.4107$. In contrast, for the PBC case, the term $\Lambda - \frac{3t^2 - \frac{1}{9}\gamma_\mathrm{d}^2}{\Lambda}$ undergoes a sharp change in its growth rate near the peak. The maximum value of the Liouvillian gap is found at $\gamma_{\mathrm{d}(\mathrm{PBC})} = 3.4709$ with $\Delta_{(\mathrm{PBC})} = 1.7320$.

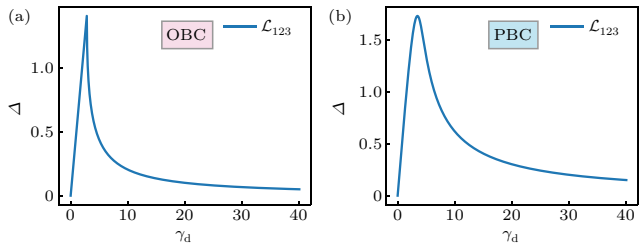


Fig. 8. Liouvillian gap Δ as a function of the dissipation rate γ_d under (a) OBC and (b) PBC, with system parameters $N = 3$, $t = 1$, and $\gamma_\mathrm{d} \in [0, 40]$. In both cases, the peak of the Liouvillian gap occurs within the range $\gamma_\mathrm{d} \in [0, 5]$. However, the peak under PBC is significantly higher than that under OBC. Regarding the shape, the Liouvillian gap Δ under OBC exhibits steep slope variations on both sides of the peak, resulting in a sharper profile, while the peak under PBC is smoother.

3.4. The case of $\mathcal{L}_{13}$

Building on the previous configuration where the set $\{j\}$ spans all lattice sites, we now weaken the dissipation on the middle site by reducing its jump strength to zero, effectively transitioning the system to the $\mathcal{L}_{13}$ configuration. Solving the master equation $\mathrm{d}\rho/\mathrm{d}t = \mathcal{L}_{13}\rho$ from the initial state $\rho_{\mathrm{ini},1} = |\varphi_{0,1}\rangle\langle\varphi_{0,1}|$, we obtain the time evolution shown in Fig. 9. The results indicate that under both OBC and PBC, the system evolves toward the same unique NESS, which remains the maximally mixed state $\rho_\mathrm{ss} = I/3$.

As before, we investigate how the Liouvillian gap Δ behaves under both boundary conditions as a function of γ_d, as shown in Fig. 10. Numerically, we find that the Δ–γ_d curve for $\mathcal{L}_{13}$ under OBC is identical to that of $\mathcal{L}_2$. We identified the underlying mechanism by block-diagonalizing the Liouvillian into symmetry sectors using parity symmetry. The first excited states are confined within 4×4 subspaces, explicitly given as

$$\mathcal{L}_2^{(4\times4)} = \begin{pmatrix} -\frac{1}{2}\gamma & \mathrm{i}t & 0 & -\mathrm{i}t \\ \mathrm{i}t & 0 & \mathrm{i}t & 0 \\ 0 & \mathrm{i}t & -\frac{1}{2}\gamma & \mathrm{i}t \\ -\mathrm{i}t & 0 & \mathrm{i}t & 0 \end{pmatrix}, \tag{48}$$

$$\mathcal{L}_{13}^{(4\times4)} = \begin{pmatrix} -\frac{1}{2}\gamma & \mathrm{i}t & 0 & -\mathrm{i}t \\ \mathrm{i}t & -\gamma & \mathrm{i}t & 0 \\ 0 & \mathrm{i}t & -\frac{1}{2}\gamma & \mathrm{i}t \\ -\mathrm{i}t & 0 & \mathrm{i}t & 0 \end{pmatrix}. \tag{49}$$

For $\mathcal{L}_{13}^{(4\times4)}$, we find that its first excited state is $\left(-4\mathrm{i}\frac{t}{\gamma+4\sqrt{\frac{1}{16}\gamma^2-2t^2}} \quad 0 \quad 4\mathrm{i}\frac{t}{\gamma+4\sqrt{\frac{1}{16}\gamma^2-2t^2}} \quad 1 \right)^\mathrm{T}$, which has a zero component along the second basis vector. Consequently, the second diagonal entry of the matrix (i.e., the $(2,2)$ element, whether it is 0 or $-\gamma$) does not affect the eigenvalue of this state. This explains why variations in that matrix element have no impact on the corresponding eigenvalue. In both cases, the Liouvillian gap Δ is given analytically as

$$\Delta_{(\mathrm{OBC})} = \left| \mathrm{Re}\left[\sqrt{\frac{1}{16}\gamma_\mathrm{d}^2 - 2t^2} - \frac{1}{4}\gamma_\mathrm{d} \right] \right|. \tag{50}$$

In contrast, under PBC, the Δ–γ_d curves of $\mathcal{L}_{13}$ and $\mathcal{L}_2$ differ. This discrepancy can be understood from the rotational symmetry previously discussed: when the jump operator acts on a single site, the configurations $\mathcal{L}_1$, $\mathcal{L}_2$, and $\mathcal{L}_3$ are related via cyclic rotations, e.g., $\mathcal{R}\mathcal{L}_1\mathcal{R}^{-1} = \mathcal{L}_2$, $\mathcal{R}\mathcal{L}_2\mathcal{R}^{-1} = \mathcal{L}_3$, and so on. As a consequence, their corresponding Δ–γ_d curves are identical. However, $\mathcal{L}_{13}$ includes dissipation on two sites, breaking this cyclic equivalence and leading to a distinct gap behavior under PBC.

Interestingly, we also observe the relations $\mathcal{R}\mathcal{L}_{12}\mathcal{R}^{-1} = \mathcal{L}_{13}$, $\mathcal{R}\mathcal{L}_{13}\mathcal{R}^{-1} = \mathcal{L}_{23}$, and $\mathcal{R}\mathcal{L}_{23}\mathcal{R}^{-1} = \mathcal{L}_{12}$, where each configuration corresponds to dissipation on two of the three sites. This further confirms that for a fixed number of quantum jump operators, the rotational symmetry ensures that the gap behavior is independent of their specific positions. Furthermore, as shown in Fig. 11, the peak of the Liouvillian gap becomes sharper and larger in magnitude as the number of dissipative sites increases. Using parity symmetry, we derive the analytical expression for the Liouvillian gap Δ in the PBC case for $\mathcal{L}_{13}$ as

$$\Delta_{(\mathrm{PBC})} = \left| \mathrm{Re}\left[\frac{1}{4}\sqrt{2\gamma_\mathrm{d}^2 + 2\Lambda - 72t^2} - \frac{1}{2}\gamma_\mathrm{d} \right] \right|, \tag{51}$$

where

$$\Lambda = \sqrt{1296t^4 - 56t^2\gamma_\mathrm{d}^2 + \gamma_\mathrm{d}^4}. \tag{52}$$

The numerical maximum of the gap is found at $\gamma_{\mathrm{d}(\mathrm{PBC})} = 5.4000$, with a peak value $\Delta_{(\mathrm{PBC})} = 1.2939$.

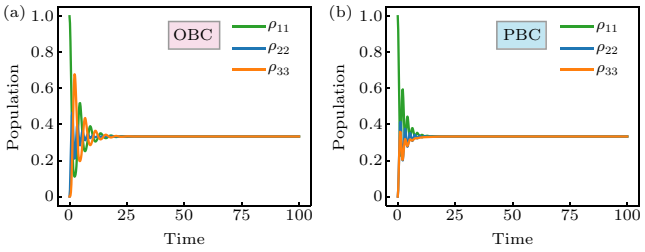


Fig. 9. Time evolution of the particle number densities ρ_{11}, ρ_{22}, and ρ_{33} under (a) OBC and (b) PBC, with system parameters $N = 3$, $t = 1$, and $\gamma_d = 1$. Notably, the amplitude ranges differ significantly: under OBC, all three densities oscillate around the value $1/3$, whereas under PBC, ρ_{11} and ρ_{22} tend to oscillate above $1/3$, while ρ_{33} oscillates below. The relaxation times are short in both cases, with the system under OBC relaxing slightly more slowly than under PBC. In the long-time limit, all three densities converge to the same NESS value, $\rho_{11} = \rho_{22} = \rho_{33} = 1/3$, for both boundary conditions.

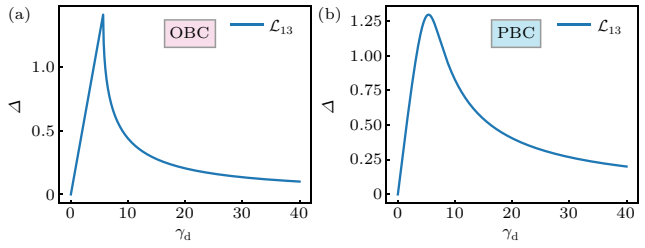


Fig. 10. Dependence of the Liouvillian gap Δ on γ_d under OBC (a) and PBC (b), with $N = 3$, $t = 1$, and γ_d ranging from 0 to 40. The peak in Δ appears near $\gamma_d = 5$ for both OBC and PBC. The OBC case exhibits sharper slope variations on either side of the peak compared to the PBC case.

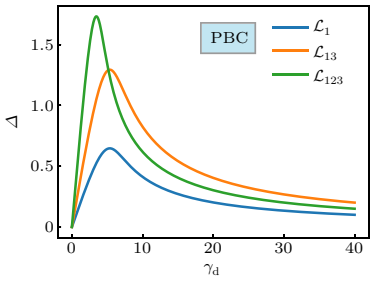


Fig. 11. Variation of the Liouvillian gap Δ for $\mathcal{L}_1$, $\mathcal{L}_{13}$, and $\mathcal{L}_{123}$ as a function of γ_d, with $N = 3$, $t = 1$, and γ_d ranging from 0 to 40. The peaks in Δ occur at distinct values of γ_d for each case, with the curves for $\mathcal{L}_{13}$ and $\mathcal{L}_{123}$ exhibiting an intersection. As the number of jump terms increases, the peak in the Liouvillian gap Δ becomes more pronounced, characterized by larger peak values and sharper profiles.

4. Type II: hopping model ($\alpha = \mathrm{R}, \mathrm{L}$)

In this section, we turn to the second type of quantum jump operator. For simplicity, our analysis is restricted to the case of $N = 3$; however, the main conclusions remain valid for larger systems.

4.1. The case of $\mathcal{L}_{123(\mathrm{R,L})}$

We modify the structure of the quantum jump operators such that both $L_{\mathrm{R},j}$ and $L_{\mathrm{L},j}$ act on all lattice sites. Figure 12 shows the time evolution of the system under both OBC and PBC, starting from the initial state $\rho_{\mathrm{ini},1} = |\varphi_{0,1}\rangle\langle\varphi_{0,1}|$.

It is evident that the two setups lead to distinct NESSs: under OBC, the system exhibits a skin effect,[25] where particles accumulate near the right boundary due to the asymmetry $\gamma_R > \gamma_L$. The corresponding NESS is

$$\rho_{\mathrm{ss(OBC)}} = \begin{pmatrix} 0.27136 & -0.05397\mathrm{i} & -0.01199 \\ 0.05397\mathrm{i} & 0.32683 & -0.06297\mathrm{i} \\ -0.01199 & 0.06297\mathrm{i} & 0.4018 \end{pmatrix}. \quad (53)$$

In contrast, under PBC, the NESS corresponds to a uniform particle distribution, $\rho_{\mathrm{ss(PBC)}} = I/3$, with equal population probability $1/3$ on each site.

We numerically solve the master equation under both boundary conditions and plot in Fig. 13 the Liouvillian gap Δ as a function of the ratio γ_L/γ_R. In both OBC and PBC cases, the Δ–γ_L/γ_R curves exhibit a near-linear increasing trend, in sharp contrast to the peak structures observed in type I. Due to the lack of symmetry induced by asymmetric jump processes, the Liouvillian spectrum is no longer analytically solvable. To gain insight, we examine how the spectrum evolves as a function of the hopping amplitude t.

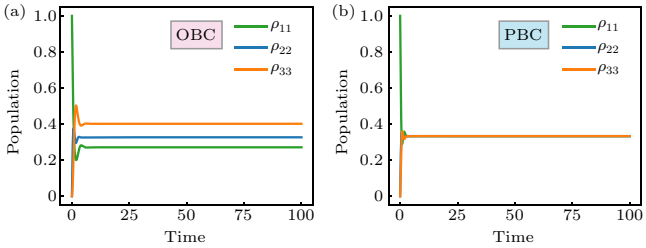


Fig. 12. Time evolution of particle number densities ρ_{11}, ρ_{22}, and ρ_{33} under OBC (a) and PBC (b), with $N = 3$, $t = 1$, $\gamma_R = 1$, and $\gamma_L = 0.5$. The oscillation amplitudes of ρ_{11}, ρ_{22}, and ρ_{33} under OBC are larger than those under PBC, with non-overlapping ranges. The NESS under OBC shows particles distributed across all three sites, with a skin effect leading to accumulation near the right boundary. In contrast, under PBC, the oscillation ranges overlap, and the NESS exhibits a uniform particle distribution with probability $1/3$ per site. The relaxation time under OBC is longer than under PBC, indicating that the system reaches the NESS more rapidly in the PBC case.

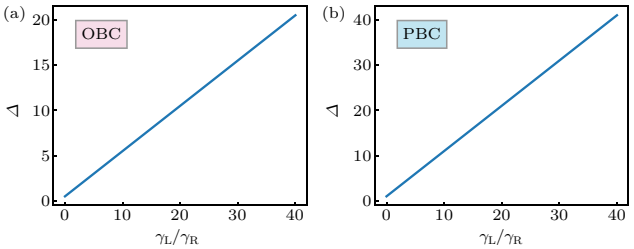


Fig. 13. Liouvillian gap Δ as a function of γ_L/γ_R under OBC (a) and PBC (b). Parameters: $N = 3$, $t = 1$, $\gamma_R = 1$, with γ_L varying from 0 to 40. In both cases, Δ exhibits an approximately linear increase with γ_L/γ_R, with the slope under PBC larger than that under OBC; specifically, the slopes are 1 and $1/2$, respectively.

Numerically, we observe that under OBC, the $\Delta_{(\mathrm{OBC})}$–γ_L/γ_R curve for small t (approaching zero) closely resembles the $t = 0$ case, maintaining a linear growth pattern. This justifies using the exact analytical solution at $t = 0$ as a good approximation for the behavior at small t. Under PBC, the $\Delta_{(\mathrm{PBC})}$–γ_L/γ_R curve remains exactly the same for all values of t. Therefore, the $t = 0$ analytical solution precisely captures the behavior of the Liouvillian gap across the entire parameter range. In this spirit, the Liouvillian gap Δ for

OBC and PBC can be expressed as $\Delta_{(\mathrm{OBC})} = \frac{1}{2}(\gamma_\mathrm{L} + \gamma_\mathrm{R})$ and $\Delta_{(\mathrm{PBC})} = \gamma_\mathrm{L} + \gamma_\mathrm{R}$, respectively. These analytical results perfectly describe the linear growth trends observed in Fig. 14.

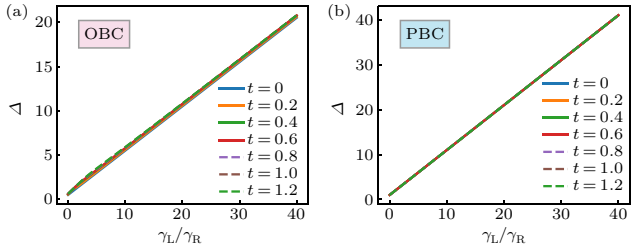


Fig. 14. Liouvillian gap Δ as a function of $\gamma_\mathrm{L}/\gamma_\mathrm{R}$ under OBC (a) and PBC (b). Parameters: $N = 3$, $\gamma_\mathrm{R} = 1$, $\gamma_\mathrm{L} \in [0, 40]$, and t takes values $\{0, 0.2, 0.4, 0.6, 0.8, 1.0, 1.2\}$. For OBC, the Δ curves as a function of $\gamma_\mathrm{L}/\gamma_\mathrm{R}$ for different t values nearly overlap within a small range, closely resembling the $t = 0$ curve. In contrast, under PBC, the curves are completely unaffected by t and remain identical to the $t = 0$ case.

4.2. The case of $\mathcal{L}_{13(\mathrm{R,L})}$

Beyond the uniform coverage of jump operators over all lattice sites, one can also design custom configurations of dissipative processes. As an example, we consider a setup where the indices $j = 1$ and 3 are selected — effectively implementing a driving from both ends toward the center. Figure 15 shows the time evolution starting from the initial state $\rho_{\mathrm{ini},1} = |\varphi_{0,1}\rangle\langle\varphi_{0,1}|$. Despite the asymmetry $\gamma_\mathrm{R} > \gamma_\mathrm{L}$, the inward driving from both ends dominates the dynamics, and the system converges to a NESS with enhanced population in the center and lower occupation at the boundaries. The numerically obtained NESSs under OBC and PBC are

$$\rho_{\mathrm{ss(OBC)}} = \begin{pmatrix} 0.22295 & 0.11148\mathrm{i} & 0.23607 \\ -0.11148\mathrm{i} & 0.51475 & -0.06557\mathrm{i} \\ 0.23607 & 0.06557\mathrm{i} & 0.26230 \end{pmatrix}, \tag{54}$$

$$\rho_{\mathrm{ss(PBC)}} = \begin{pmatrix} 0.249 & -0.132-0.084\mathrm{i} & 0.119+0.005\mathrm{i} \\ -0.132+0.084\mathrm{i} & 0.536 & -0.106+0.094\mathrm{i} \\ 0.119-0.005\mathrm{i} & -0.106-0.094\mathrm{i} & 0.215 \end{pmatrix}. \tag{55}$$

As shown in Fig. 16, the resulting Liouvillian gap Δ displays qualitatively different behaviors under OBC and PBC: under OBC, the gap shows a clear non-monotonic structure with a peak; in contrast, the PBC case continues to show a nearly linear increase in Δ as a function of $\gamma_\mathrm{L}/\gamma_\mathrm{R}$. This is expected, since under PBC the structure effectively introduces hopping between sites 1 and 3, maintaining a form of uniform dissipation-induced mixing. Evidently, the Liouvillian spectrum remains analytically intractable. Therefore, as in earlier sections, we adopt a perturbative approach[32,33] to approximate the Δ–$\gamma_\mathrm{L}/\gamma_\mathrm{R}$ behavior. This approximation remains valid particularly in the small t limit, where dissipative effects dominate the dynamics. The detailed derivation is provided in the Appendix A. As shown there, the solution corresponding to the blue dashed line is given by

$$\Delta_{(\mathrm{blue})} = \frac{1}{4}\gamma_\mathrm{L} + \frac{1}{4}\gamma_\mathrm{R}, \tag{56}$$

while the green dashed line corresponds to

$$\Delta_{(\mathrm{green})} = \frac{1}{2}\gamma_\mathrm{R} + \frac{2t^2}{\gamma_\mathrm{L}}. \tag{57}$$

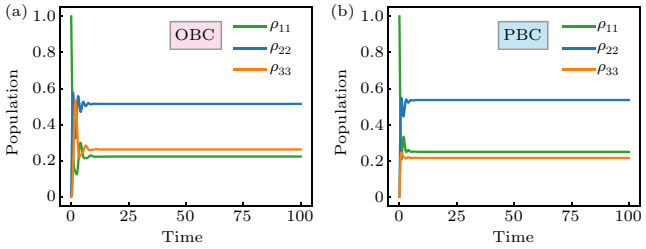


Fig. 15. Time evolution of particle number densities ρ_{11}, ρ_{22}, and ρ_{33} under OBC (a) and PBC (b). Parameters: $N = 3$, $t = 1$, $\gamma_\mathrm{R} = 1$, $\gamma_\mathrm{L} = 0.5$. In both cases, the system reaches a NESS distribution with nonzero occupation on all three sites, characterized by a peak at the center ρ_{22} and lower values at the edges ρ_{11} and ρ_{33}, forming a "center-high, edge-low" profile. In terms of relaxation time, the system under OBC relaxes more slowly compared to PBC, indicating that PBC facilitates faster convergence to the NESS.

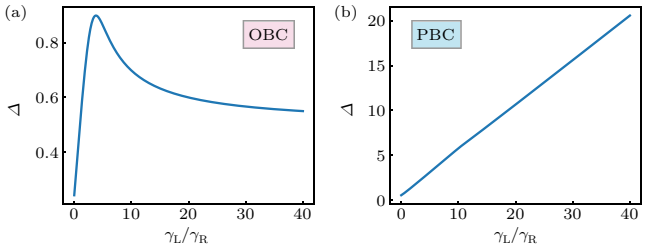


Fig. 16. Liouvillian gap Δ as a function of $\gamma_\mathrm{L}/\gamma_\mathrm{R}$ under OBC (a) and PBC (b). Parameters: $N = 3$, $t = 1$, $\gamma_\mathrm{R} = 1$, $\gamma_\mathrm{L} \in [0, 40]$. The Δ–$\gamma_\mathrm{L}/\gamma_\mathrm{R}$ curves exhibit starkly different behaviors: under OBC, Δ shows a peak near $\gamma_\mathrm{L}/\gamma_\mathrm{R} = 5$, while under PBC, it displays a monotonically linear increase. These differences highlight the distinct spectral responses induced by boundary conditions in the presence of asymmetric dissipation.

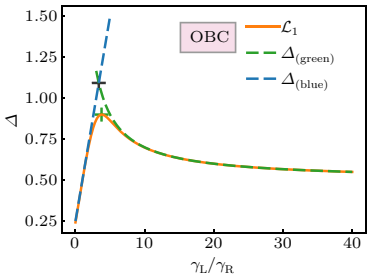


Fig. 17. Comparison of Δ as a function of $\gamma_\mathrm{L}/\gamma_\mathrm{R}$ between approximate and numerical solutions under OBC. Blue and green dashed lines denote approximate solutions obtained via perturbation methods, while the orange solid line represents the numerical solution. Parameters: $N = 3$, $t = 1$, $\gamma_\mathrm{R} = 1$, $\gamma_\mathrm{L} \in [0, 40]$. Green and black "+" symbols mark the peak values from the numerical and perturbative solutions, respectively, with corresponding parameters $\gamma_\mathrm{L}/\gamma_{\mathrm{R(green)}} = 3.7675$, $\Delta_{\mathrm{(green)}} = 0.9$ and $\gamma_\mathrm{L}/\gamma_{\mathrm{R(black)}} = 3.3723$, $\Delta_{\mathrm{(black)}} = 1.0931$. The close agreement between approximate and numerical solutions partially explains the origin of the peak in the Δ–$\gamma_\mathrm{L}/\gamma_\mathrm{R}$ curve for $\mathcal{L}_{13}$. In both the small and large $\gamma_\mathrm{L}/\gamma_\mathrm{R}$ regimes, Δ follows the trends predicted by the respective approximate solutions, further validating the inevitability of the peak formation.

The comparison between the numerical solution and the analytical approximations is shown in Fig. 17, where we observe excellent agreement between the approximate expressions and the numerical data. Under PBC, the Liouvillian gap Δ can be approximately obtained in the limit $t = 0$, yielding

$$\Delta_{(\mathrm{PBC})} = \frac{1}{2}\gamma_{\mathrm{L}} + \frac{1}{2}\gamma_{\mathrm{R}}. \tag{58}$$

5. Summary

We have conducted a detailed study of relaxation dynamics and NESS properties in finite one-dimensional fermionic lattices subject to Lindblad dissipation. By systematically varying both the form of the jump operators and the boundary conditions, we have uncovered several key features.

(i) Multiple zero modes of the Liouvillian superoperator may coexist, some yielding unphysical density matrices. We demonstrated that the true NESS is the physically admissible superposition of these modes, selected by the overlap of the initial state with the Liouvillian eigenbasis.

(ii) Across all dissipation patterns, including single-site dephasing, directional hopping, full-site coverage, and partial coverage, the Liouvillian gap Δ exhibits a pronounced peak as a function of the dissipation strength γ_{d}. This peak corresponds to the shortest relaxation time and arises from spectral transitions, such as the splitting of purely imaginary eigenvalues into complex conjugate pairs. It marks a regime where the dissipation rate and coherent strength are optimally balanced. This dynamic equilibration is governed by parity symmetry, which is preserved under both PBC and OBC.

(iii) Parity and rotation symmetries enable analytic block-diagonalization of $\mathcal{L}$ and enforce identical Δ–γ_{d} curves among cyclically related jump configurations under PBC. While OBC yields a unique, symmetry-determined NESS (often the maximally mixed state), PBC may support initial-state–dependent mixtures of zero modes and, in asymmetric hopping, a pronounced skin effect with particle accumulation.

(iv) In both the weak-hopping ($t \ll \gamma_{\mathrm{d}}$) and weak-dissipation ($\gamma_{\mathrm{d}} \ll t$) limits, non-Hermitian perturbation theory provides closed-form expressions for the first excited Liouvillian eigenvalue λ_1. These simple formulas reproduce the rising and falling segments of the Δ–γ curves with excellent accuracy. Our results deepen the understanding of how dissipation geometry, coupling strength, and system symmetry collectively shape nonequilibrium behavior in finite quantum systems. They further provide practical guidelines for engineering dissipative protocols, including the strategic placement of quantum jump operators and the careful choice of boundary conditions,[36,37] to effectively control relaxation times and NESS preparation in quantum simulators and other open quantum platforms.

Appendix A

A1. Derivation of the value of the peak in the dephasing model

We first treat the tunneling amplitude t as a perturbation in order to obtain approximate eigenvalues for $\mathcal{L}_1$ (noting that $\mathcal{L}_1$ and $\mathcal{L}_3$ yield identical spectral behavior due to parity symmetry, as discussed earlier). Using the vectorized representation of the density matrix, the Liouvillian $\mathcal{L}_1$ can be decomposed into an unperturbed part $\mathcal{L}^{(0)}$ and a perturbation $\mathcal{L}'$

$$\mathcal{L}_1 = \mathcal{L}^{(0)} + \mathcal{L}',$$

$$\mathcal{L}^{(0)} = \begin{pmatrix} 0 & 0 & 0 & 0 & 0\,0 & 0 & 0\,0 \\ 0 & -\frac{\gamma_{\mathrm{d}}}{2} & 0 & 0 & 0\,0 & 0 & 0\,0 \\ 0 & 0 & -\frac{\gamma_{\mathrm{d}}}{2} & 0 & 0\,0 & 0 & 0\,0 \\ 0 & 0 & 0 & -\frac{\gamma_{\mathrm{d}}}{2} & 0\,0 & 0 & 0\,0 \\ 0 & 0 & 0 & 0 & 0\,0 & 0 & 0\,0 \\ 0 & 0 & 0 & 0 & 0\,0 & 0 & 0\,0 \\ 0 & 0 & 0 & 0 & 0\,0 & -\frac{\gamma_{\mathrm{d}}}{2} & 0\,0 \\ 0 & 0 & 0 & 0 & 0\,0 & 0 & 0\,0 \\ 0 & 0 & 0 & 0 & 0\,0 & 0 & 0\,0 \end{pmatrix},$$

$$\mathcal{L}' = \begin{pmatrix} 0 & \mathrm{i}t & 0 & -\mathrm{i}t & 0 & 0 & 0 & 0 & 0 \\ \mathrm{i}t & 0 & \mathrm{i}t & 0 & -\mathrm{i}t & 0 & 0 & 0 & 0 \\ 0 & \mathrm{i}t & 0 & 0 & 0 & -\mathrm{i}t & 0 & 0 & 0 \\ -\mathrm{i}t & 0 & 0 & 0 & \mathrm{i}t & 0 & -\mathrm{i}t & 0 & 0 \\ 0 & -\mathrm{i}t & 0 & \mathrm{i}t & 0 & \mathrm{i}t & 0 & -\mathrm{i}t & 0 \\ 0 & 0 & -\mathrm{i}t & 0 & \mathrm{i}t & 0 & 0 & 0 & -\mathrm{i}t \\ 0 & 0 & 0 & -\mathrm{i}t & 0 & 0 & 0 & \mathrm{i}t & 0 \\ 0 & 0 & 0 & 0 & -\mathrm{i}t & 0 & \mathrm{i}t & 0 & \mathrm{i}t \\ 0 & 0 & 0 & 0 & 0 & -\mathrm{i}t & 0 & \mathrm{i}t & 0 \end{pmatrix}. \tag{A1}$$

When $t = 0$, the eigenvalues of $\mathcal{L}^{(0)}$ are $\lambda_0 = 0$ (fivefold degenerate) and $\lambda_1 = -\gamma_{\mathrm{d}}/2$ (fourfold degenerate). Projecting $\mathcal{L}'$ into the degenerate subspace of λ_0 yields a 5×5 effective perturbative matrix

$$\mathcal{L}'_{\mathrm{eff}} = \begin{pmatrix} 0 & 0 & 0 & 0 & 0 \\ 0 & 0 & \mathrm{i}t & -\mathrm{i}t & 0 \\ 0 & \mathrm{i}t & 0 & 0 & -\mathrm{i}t \\ 0 & -\mathrm{i}t & 0 & 0 & \mathrm{i}t \\ 0 & 0 & -\mathrm{i}t & \mathrm{i}t & 0 \end{pmatrix}. \tag{A2}$$

Diagonalizing this matrix gives first-order corrections $\lambda_{01}^{(1)} = -2\mathrm{i}t$, $\lambda_{02}^{(1)} = 2\mathrm{i}t$, and a threefold degenerate eigenvalue $\lambda_{03}^{(1)} = 0$. Since these are purely imaginary, they do not affect the Liouvillian gap.

Second-order corrections are computed as

$$\mathcal{L}''_{lq} = \sum_m \frac{\langle\rho_l|\mathcal{L}'|\rho_m\rangle\langle\rho_m|\mathcal{L}'|\rho_q\rangle}{\lambda_0 - \lambda_m}, \tag{A3}$$

where $|\rho_l\rangle$ and $|\rho_q\rangle$ belong to the λ_0 subspace and $|\rho_m\rangle$ are eigenstates with $\lambda_m = -\gamma_{\mathrm{d}}/2$. The resulting matrix is

$$\mathcal{L}'' = \begin{pmatrix} -\frac{4t^2}{\gamma_{\mathrm{d}}} & \frac{4t^2}{\gamma_{\mathrm{d}}} & 0 & 0 & 0 \\ \frac{4t^2}{\gamma_{\mathrm{d}}} & -\frac{4t^2}{\gamma_{\mathrm{d}}} & 0 & 0 & 0 \\ 0 & 0 & -\frac{2t^2}{\gamma_{\mathrm{d}}} & 0 & 0 \\ 0 & 0 & 0 & -\frac{2t^2}{\gamma_{\mathrm{d}}} & 0 \\ 0 & 0 & 0 & 0 & 0 \end{pmatrix}. \tag{A4}$$

Hence, the second-order corrections are $\lambda_{01}^{(2)} = -2t^2/\gamma_{\rm d}$ (twice degenerate), $\lambda_{02}^{(2)} = -8t^2/\gamma_{\rm d}$ (twice degenerate), and $\lambda_{03}^{(2)} = 0$. The approximate Liouvillian gap is thus $\Delta_{\rm orange} = |\lambda_{01}^{(2)}| = 2t^2/\gamma_{\rm d}$.

Treating $\gamma_{\rm d}$ as a perturbation in the $t \gg \gamma_{\rm d}$ limit gives first-order corrections $|\lambda_{11}^{(1)}| = 0.125\gamma_{\rm d}$, which matches the left side of the peak in Fig. 6.

A2. Derivation of the Liouvillian gap in the hopping model for $\mathcal{L}_{13({\rm R,L})}$

In the weak-coupling limit (t as a perturbation), the Liouvillian can be written as

$$\mathcal{L}_{13({\rm R,L})} = \mathcal{L}^{(0)}_{13({\rm R,L})} + \mathcal{L}'_{13({\rm R,L})}, \tag{A5}$$

with unperturbed and perturbation matrices

$$\mathcal{L}^{(0)}_{13({\rm R,L})} = \begin{pmatrix} -\gamma_{\rm R} & 0 & \cdots & 0 \\ 0 & -\frac{1}{2}\gamma_{\rm R} & \cdots & 0 \\ \vdots & \vdots & \ddots & \vdots \\ \gamma_{\rm R} & 0 & \cdots & -\gamma_{\rm L} \end{pmatrix},$$

$$\mathcal{L}'_{13({\rm R,L})} = \begin{pmatrix} 0 & {\rm i}t & \cdots & 0 \\ {\rm i}t & 0 & \cdots & 0 \\ \vdots & \vdots & \ddots & \vdots \\ 0 & 0 & \cdots & 0 \end{pmatrix}. \tag{A6}$$

For $t = 0$, the eigenvalues are

$$\begin{aligned} &\lambda_0^{(0)} = 0, \quad \lambda_1^{(0)} = -\gamma_{\rm R}, \quad \lambda_2^{(0)} = -\gamma_{\rm L}, \\ &\lambda_3^{(0)} = -\frac{1}{2}\gamma_{\rm R}\ \text{(double)}, \quad \lambda_4^{(0)} = -\frac{1}{2}\gamma_{\rm L}\ \text{(double)}, \\ &\lambda_5^{(0)} = -\frac{1}{2}(\gamma_{\rm L}+\gamma_{\rm R})\ \text{(double)}. \end{aligned} \tag{A7}$$

First-order corrections vanish. Using second-order perturbation theory with biorthogonal eigenvectors, we obtain

$$\lambda_0^{(2)} = -\frac{4t^2}{\gamma_{\rm L}} - \frac{4t^2}{\gamma_{\rm R}}, \quad \lambda_{3,1}^{(2)} = -2\frac{t^2}{\gamma_{\rm L}},$$

$$\lambda_{3,2}^{(2)} = -\left(\frac{8t^2}{\gamma_{\rm R}} + \frac{2t^2}{\gamma_{\rm L}}\right), \tag{A8}$$

$$\lambda_{4,1}^{(2)} = -2\frac{t^2}{\gamma_{\rm R}}, \quad \lambda_{4,2}^{(2)} = -\frac{1}{\gamma_{\rm L}\gamma_{\rm R}}(2t^2\gamma_{\rm L} + 8t^2\gamma_{\rm R}), \tag{A9}$$

$$\lambda_{5,1}^{(2)} = \lambda_{5,2}^{(2)} = \frac{2t^2}{\gamma_{\rm R}} + \frac{2t^2}{\gamma_{\rm L}}. \tag{A10}$$

In the weak-dissipation limit ($\gamma_{\rm L,R} \ll t$), the first-order correction to the triply degenerate zero mode is

$$|\lambda_{01}^{\prime(1)}| = \frac{1}{4}\gamma_{\rm L} + \frac{1}{4}\gamma_{\rm R}. \tag{A11}$$

Hence, the Liouvillian gap is captured by

$$\Delta_{\rm green} = \frac{1}{2}\gamma_{\rm R} + 2\frac{t^2}{\gamma_{\rm L}}, \quad \Delta_{\rm blue} = \frac{1}{4}\gamma_{\rm L} + \frac{1}{4}\gamma_{\rm R}, \tag{A12}$$

matching the right and left sides of the peak in Fig. 17.

Data availability statement

The data that support the findings of this study are openly available at https://doi.org/10.57760/sciencedb.j00113.00254.

Acknowledgment

This project was supported by the National Natural Science Foundation of China (Grant Nos. 12275193 and 11975166).

References

[1] Impertro A, Huh S J, Karch S, Wienand J F, Bloch I and Aidelsburger M 2025 *Nat. Phys.* **21** 895
[2] Wang X Q, Luo G Q, Liu J Y, Liu W V, Hemmerich A and Xu Z F 2021 *Nature* **596** 227
[3] Yang B, Sun H, Huang C J, Wang H Y, Deng Y, Dai H N, Yuan Z S and Pan J W 2020 *Science* **369** 550
[4] Singh J, Reuter J A P, Calarco T, Motzoi F and Zeier R 2025 arXiv:2503.06768 [quant-ph]
[5] Jiang L, Xu Y, Li S, *et al.* 2025 *Phys. Rev. Appl.* **24** 034057
[6] Liu C H, Ballard A, Olaya D, Schmidt D R, Biesecker J, Lucas T, Ullom J, Patel S, Rafferty O, Opremcak A and Dodge K 2023 *Phys. Rev. X* **4** 030310
[7] Zhang P, Dong H, Gao Y, Zhao L, Hao J, Desaules J Y, Guo Q, Chen J, Deng J, Liu B and Ren W 2023 *Nat. Phys.* **19** 120
[8] Wu Z, Hu C, Wang T, Chen Y, Li Y, Zhao L, Lü X Y and Peng X 2024 *Phys. Rev. Lett.* **133** 173602
[9] Mahdian M and Mousavi Z 2025 *Scientific Reports* **15** 11931
[10] Haga T, Nakagawa M, Hamazaki R and Ueda M 2023 *Phys. Rev. Res.* **5** 043225
[11] Guo Y C and Yang S 2024 *Chin. Phys. Lett.* **41** 120302
[12] Zhao J, Liu Y, Qin H, Chen Z and Zhao C 2021 *Phys. Rev. Lett.* **127** 123901
[13] Bałut D, Bradlyn B and Abbamonte P 2025 *Phys. Rev. B* **111** 12
[14] Bhattacharya A and Raman C 2025 *Phys. Rev. Lett.* **134** 080201
[15] Xiong S J, Sun Z and Wang X G 2023 *Chin. Phys. B* **32** 080302
[16] Mori T and Shirai T 2020 *Phys. Rev. Lett.* **125** 230604
[17] Zhou K J, Zou J and Shao B 2023 *Phys. Rev. A* **108** 042206
[18] Rahmani A, Opala A and Matuszewski M 2024 *Phys. Rev. B* **109** 085311
[19] Lidar D A 2019 arXiv:1902.00967 [quant-ph]
[20] Lindblad G 1976 *Commun. Math. Phys.* **48** 119
[21] Sieberer L M, Buchhold M and Diehl S 2016 *Rep. Prog. Phys.* **79** 096001
[22] Yuan D, Wang H R, Wang Z and Deng D L 2021 *Phys. Rev. Lett.* **126** 160401
[23] Albert V V, Bradlyn B, Fraas M and Jiang L 2016 *Phys. Rev. X* **6** 041031
[24] Kanki K, Hashimoto K, Petrosky T and Tanaka S 2016 *15th International Conference on Non-Hermitian Hamiltonians in Quantum Physics* 18–23 May 2015 Palermo, Italy 289
[25] Minganti F, Biella A, Bartolo N and Ciuti C 2018 *Phys. Rev. A* **98** 042118
[26] Manzano D and Hurtado P I 2018 *Adv. Phys.* **67** 1
[27] Haga T, Nakagawa M, Hamazaki R and Ueda M 2021 *Phys. Rev. Lett.* **127** 070402
[28] Casteels W, Fazio R and Ciuti C 2017 *Phys. Rev. A* **95** 012128
[29] Turkeshi X and Schiró M 2021 *Phys. Rev. B* **104** 144301
[30] Temme K, Wolf M M and Verstraete F 2012 *New J. Phys.* **14** 075004
[31] Ashida Y, Furukawa S, Ueda M 2017 *Nat. Commun.* **8** 15791
[32] Griffiths D J and Schroeter D F 2005 *Introduction to Quantum Mechanics* (New York: Prentice Hall) pp. 279–294
[33] Sakurai J J and Napolitano J 2021 *Modern Quantum Mechanics* (San Francisco: Addison-Wesley) pp. 252–255
[34] Cohen-Tannoudji C, Diu B and Laloë F 1977 *Quantum Mechanics* (New York: John Wiley & Sons) Vol. 1 pp. 312–314
[35] Dresselhaus M S, Dresselhaus G and Jorio A 2007 *Group Theory: Application to the Physics of Condensed Matter* (Berlin: Springer Science & Business Media) pp. 31–40
[36] Minev Z K, Mundhada S O, Shankar S, Reinhold P, Gutiérrez-Jáuregui R, Schoelkopf R J and Devoret M H 2019 *Nature* **570** 200
[37] Zhao S K, Ge Z Y, Ang Z, Xue G M, Yan H S, Wang Z T and Zhao S P 2022 *Phys. Rev. Lett.* **129** 160602